

Development and Testing of an All-Atom Force Field for Diketopyrrolopyrrole Polymers with Conjugated Substituents

Vivek Sundaram, Alexey V. Lyulin, and Björn Baumeier*

Cite This: *J. Phys. Chem. B* 2020, 124, 11030–11039

Read Online

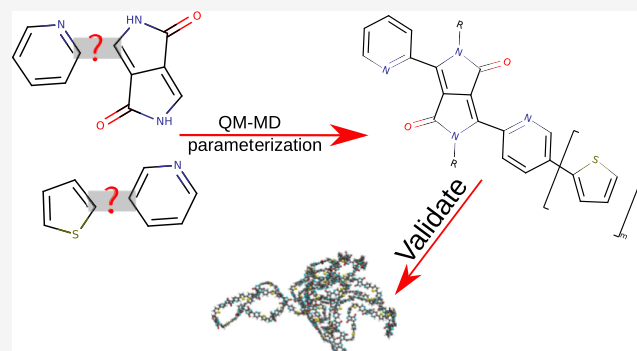
ACCESS |

Metrics & More

Article Recommendations

Supporting Information

ABSTRACT: We develop an all-atom force field for a series of diketopyrrolopyrrole polymers with two aromatic pyridine substituents and a variable number of π -conjugated thiophene units in the backbone (DPP2PymT), used as donor materials in organic photovoltaic devices. Available intrafragment parameterizations of the individual fragment building blocks are combined with interfragment bonded and nonbonded parameters explicitly derived from density functional theory calculations. To validate the force field, we perform classical molecular dynamics simulations of single polymer chains with $m = 1, 2, 3$ in good and bad solvents and of melts. We observe the expected dependence of the chain conformation on the solvent quality, with the chain collapsing in water, and swelling in chloroform. The glass-transition temperature for the polymer melts is found to be in the range of 340–370 K. Analysis of the mobility of the conjugated segments in the polymer backbone reveals two relaxation processes: a fast one with a characteristic time at room temperature on the order of 10 ps associated with nearly harmonic vibrations and a slow one on the order of 100 ns associated with temperature-activated cis–trans transitions.



1. INTRODUCTION

The theoretical maximum power conversion efficiency (PCE) of a single-junction solar cell is 33.7%, as defined by the Shockley–Queisser limit.^{1,2} The majority of currently available solar cells are based on silicon and deliver a PCE of up to 26%,^{3–6} which is about 80% of the Shockley–Queisser limit. Obtaining such high conversion efficiencies requires, however, monocrystalline wafers whose processing causes high production costs. In contrast, devices made from less expensive polycrystalline or amorphous silicon wafers show a reduction of the PCE to around 10–14%.^{7,8} Instead of using inorganic materials, the use of organic molecules (either polymers or small molecules) in photovoltaic devices is attractive because of their ease of processing from solutions, higher flexibility due to a low bulk modulus, and the nontoxicity of the compounds used.^{9,10} Low dielectric screening and substantial disorder in the materials generally lead to strongly bound, localized electronic excitations, hampering the efficient generation of free charge carriers and their transport processes in donor–acceptor heterojunctions. To overcome these factors limiting the PCE of organic photovoltaic devices, significant effort is directed toward tuning electronic and structural properties of the materials by altering the architecture of donor and acceptor compounds.^{9,11,12}

Among the intensively studied donor materials are polymers based on diketopyrrolopyrroles (DPPs),^{4,13–15} see the monomer unit in Figure 1. They can be easily modified by adding various aromatic and π -conjugated substituents to the

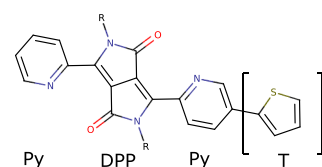


Figure 1. Chemical structure of a DPP2PymT monomer unit consisting of four individual components: two Py rings, one DPP fused ring, and one thiophene (T) ring, while m denotes the number of thiophene units. R represents 2-hexyldecyl.

backbone and different side chains to DPP, affecting both the solubility and crystallinity of the polymer as well as its electronic properties. With suitably chosen substituents, a low-band-gap internal donor–acceptor architecture leads to efficient harvesting of the solar energy spectrum and a PCE of around 8% in blends with fullerene acceptors.^{16–19}

To guide the rational design of such block copolymers for further increasing the PCE, insight into how their internal architecture and the blend morphology affect the electronic

Received: July 24, 2020

Revised: November 5, 2020

Published: November 19, 2020



conversion and transport processes in a solar cell's active layer is often sought via multiscale simulation approaches which link structural features on meso- and microscopic scales with electronic dynamics.^{20–25} A key element of such approaches is the simulation of representative structures with atomistic detail, which on the needed scale can only be obtained with classical molecular dynamics (MD). The resulting morphologies must not only reliably reflect the overall conformational details of the polymer chains in the bulk and at the interface to the acceptor but also accurately capture the dynamics of torsional degrees of freedom between the segments in the individual chains as these can massively influence the localization characteristics of electronic states and, hence, their dynamics.^{26–28} This, in turn, requires the availability of precise classical force fields (FFs) which are parameterized for the specific chemical composition of the materials at hand.

In this work, we focus on a particular series of DPP polymers, as shown in Figure 1, with two aromatic pyridine (Py) substituents and a variable number of π -conjugated thiophene (T) units in the backbone (DPP2PymT).²⁹ The compounds are specifically chosen because when used in conjugation with PCBM[60] and PCBM[70] acceptors, a difference in the charge generation is observed depending on donor or acceptor excitation.²⁹ With the end goal to study this dichotomous role of donor or acceptor excitation, we begin performing classical simulations to study structural and segmental properties of the polymer itself. We develop an all-atom FF for this series by starting out from available intrafragment parameterizations of the individual fragment building blocks. The missing bond, angle, and dihedral bonded parameters for the interfragment degrees of freedom are derived in an iterative procedure from density functional theory (DFT) calculations using standard protocols.^{30–34} DFT is also used to refine atomic partial charges for the fully assembled DPP2PymT monomers. Guaranteeing a priori the transferability of gas-phase optimized FFs to a wide range of conditions is in general a challenging task. The bonded potentials represent the intrapolymer interactions and—unless the condensed phase dramatically changes these in the polymer by strongly affecting its electronic structure—we expect them to transfer to the condensed phase. Certain torsional motion may be constrained by interpolymer interactions, which are typically nonbonded interactions, or excluded volume effects. To scrutinize a posteriori the applicability of our FF under different conditions, we perform classical MD simulations of a single N_p -DPP2PymT chain with $N_p = 50$, $m = 1, 2, 3$, and branched 2-hexyldecyl side chains in both solutions with chloroform and water and a few of such chains as melts. We investigate in particular the swelling behavior depending on solvent quality, the glass-transition temperature, and the mobility of the conjugated segments.

This paper is organized as follows: In Section 2, we present the methodology and computational details of the iterative FF development. Details of the individual steps and the final parameterized FF are given in Section 3.1, while the results for the solution and melt simulations are reported in Sections 3.2 and 3.3, respectively. A brief summary concludes the paper.

2. METHODOLOGY

An FF represents the quantum-mechanical many-body energy of a molecular conformation, defined by the set of atomic coordinates $\{\mathbf{R}\}$, as a sum of classical interactions. The potential energy surface (PES) is then written in terms of

bonded and nonbonded interactions, $V(\{\mathbf{R}\}) = V_{\text{bonded}}(\{\mathbf{R}\}) + V_{\text{non-bonded}}(\{\mathbf{R}\})$. The nonbonded ones (Lennard-Jones and electrostatic) are pairwise additive, that is, $V_{\text{non-bonded}}(\{\mathbf{R}\}) = \sum_{i<j} V_{ij}(\mathbf{R}_{ij})$, while the bonded ones comprise 2- (bonds r_{ij}), 3- (angles θ_{ijk}), and 4-body (dihedral angles ϕ_{ijkl}) interactions.

For developing the DPP2PymT FF, we start from available parameters in the GROMOS 54A7 form for the fragment building blocks of Py, thiophene (T), and DPP,³⁵ with $R = H$ in Figure 1. These were obtained from the Automated FF Topology Builder (ATB, <http://compbio.biosci.uq.edu.au/atb>),³⁶ which extracts bond and angle parameters from the Hessian of the optimized structure and fits partial charges through the Kollmann–Singh scheme.³⁷ Lennard-Jones parameters are taken from the GROMOS 96 FF.³⁸ These intrafragment parameterizations need to be supplemented by interfragment interactions related to the linking of the units in the polymer, that is, $V_{\text{bonded}} = V_{\text{bonded}}^{\text{intra}} + V_{\text{bonded}}^{\text{inter}}$. To obtain

$$V_{\text{bonded}}^{\text{inter}} = \sum_{ij}^{\text{inter}} V_{ij}^{\text{bond}}(r_{ij}) + \sum_{ijk}^{\text{inter}} V_{ijk}^{\text{angle}}(\theta_{ijk}) + \sum_{ijkl}^{\text{inter}} V_{ijkl}^{\text{dihedral}}(\phi_{ijkl}) \quad (1)$$

we follow a step-by-step refinement procedure^{30–34} based on Py–T and DPP–Py dimer structures (see Figure 2 for atom

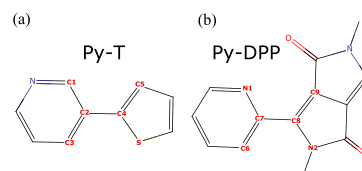


Figure 2. Structure of the (a) Py–T and (b) Py–DPP dimers, with explicit labels for atoms involved in the interfragment degrees of freedom for which FF parameters need to be determined.

definitions), respectively, as illustrated in Figure 3. The respective parameters for the T–T structures occurring for $m = 2, 3$ are taken from the literature.³⁰ From the available fragment parameterizations of DPP, Py, and T, an initial FF (FF_0) is created, in which all intermonomer bonded potentials are 0, dimer CHELPG partial charges³⁹ are assigned from a DFT calculation, and Lennard-Jones parameters are taken from the existing GROMOS FF with geometric averaging for atom pairs. Starting from FF_0 , first harmonic bond potentials are added (FF_1), then harmonic angle potentials (FF_2), and finally periodic dihedral potentials (FF_3). To determine these additions, the relevant part of the PES must be known for each individual coordinate at each step of the process. A series of calculations must be performed, in which one of the structural parameters ($x = \{r_{ij}; \theta_{ijk}; \phi_{ijkl}\}$) is constrained to a certain value, while all other degrees of freedom are optimized. Two of such relaxed PES scans are required: one with the current FF (FF_n), yielding $V^{\text{FF}_n}(x)$, and the other based on DFT calculations, yielding a reference $V^{\text{DFT}}(x)$. Then, the difference $\Delta V(x) = V^{\text{DFT}}(x) - V^{\text{FF}_n}(x)$ is calculated and used to fit the functional form of the respective potential term. With its parameters, for example, the equilibrium value and force constant for a bond, determined, the terms are added to the FF. Details will be discussed below in the specific sections.

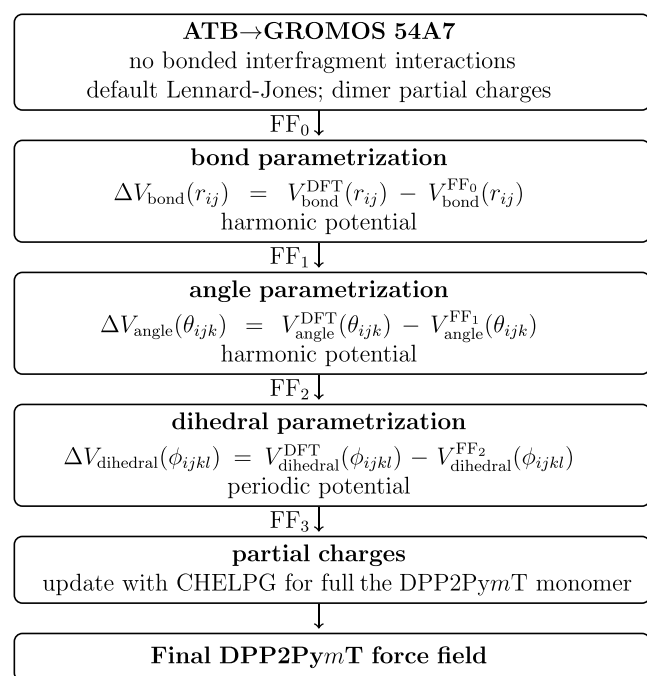


Figure 3. Illustration of the development of a N_p -DPP2PymT FF, where N_p is the degree of polymerization, based using a step-by-step procedure to add intermonomer potentials to a baseline GROMOS 54A7 monomer parameterization.

All DFT calculations used in this work have been performed with the ORCA software,⁴⁰ employing the B3LYP hybrid functional⁴¹ and the def2-TZVP basis set.⁴² See Section 3.1.3 for a brief discussion about the influence of the method and basis set on the parameterization. The VOTCA-XTP package^{21,25} has been used for the assignment of atomic partial charges with the CHELPG³⁹ method. GROMACS 2018.3^{43,44} with double precision has been used for all calculations to develop the classical FF. In the PES scans, the energy has been minimized until the force on each atom is below 0.1 kJ/mol/nm.

3. RESULTS

3.1. N_p -DPP2PymT FF. 3.1.1. Bond Stretching. As mentioned in Section 2, we first consider the two bond stretching potentials between Py-T and Py-DPP. The results of the respective PES scan on DFT/B3LYP and FF levels, FF₀ and FF₁, are shown in Figure 4. As expected, the scan with the initial FF (gray open circles) does not exhibit any minimum in both cases, while its faint linear behavior can be attributed to the nonbonded interactions as the distance between the two fragments is varied. In contrast, the DFT scans (red squares) clearly show harmonic behavior with an equilibrium bond length of $r_{ij}^0 = 1.46 \text{ \AA}$ for the bonds highlighted in the respective insets.

The difference $\Delta V_{\text{bond}}(r_{ij}) = V_{\text{bond}}^{\text{DFT}}(r_{ij}) - V_{\text{bond}}^{\text{FF}_0}(r_{ij})$ between the energy values obtained by B3LYP and FF₀ was modeled as a harmonic potential

$$V_{\text{bond}}(r_{ij}) = \frac{1}{2} k_{ij} (r_{ij} - r_{ij}^0)^2 \quad (2)$$

where k_{ij} is the harmonic force constant. However, GROMOS-96 uses a fourth-power potential

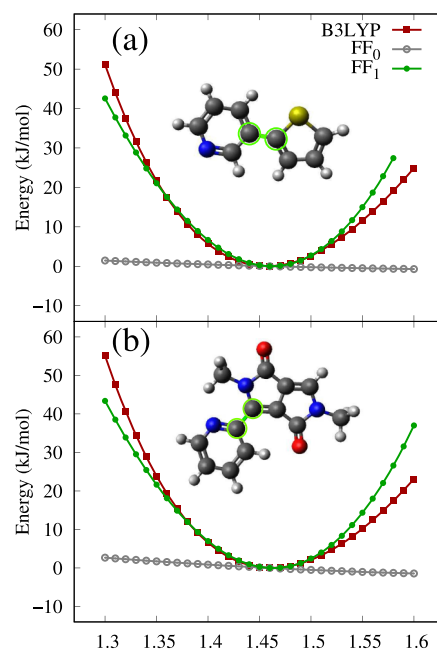


Figure 4. PES scans (in kJ/mol) for the (a) C2–C4 bond in Py–T and (b) C7–C8 bond in Py–DPP, resulting from DFT/B3LYP (red squares), the initial FF₀ parameterization (gray open circles), and the updated FF₁ (green filled circles) FFs, respectively. The unknown bonds and the atoms involved are highlighted in the insets.

$$V_{\text{bond}}(r_{ij}) = \frac{1}{4} \tilde{k}_{ij} (r_{ij}^2 - (r_{ij}^0)^2)^2 \quad (3)$$

Therefore, the determined force constant is converted according to

$$\tilde{k}_{ij} = \frac{k_{ij}}{2(r_{ij}^0)^2} \quad (4)$$

After fitting, the determined parameters as given in Table 1 have been added to the FF, defining FF₁. To validate this step,

Table 1. Determined Harmonic Parameters for the Interfragment Bond Stretching Potentials as Used in Eq 3

	$i-j$	\tilde{k}_{ij} (kJ/mol/nm ⁴)	r_{ij}^0 (nm)
Py–T	C2–C4	8.44×10^6	0.146
Py–DPP	C7–C8	3.80×10^6	0.146

the PES scans are repeated with the updated FF, yielding results shown as green filled circles in Figure 4. For both Py–T and Py–DPP, the agreement with the DFT/B3LYP reference is very good within $\pm 0.05 \text{ \AA}$ of the equilibrium bond length. The observed deviations for larger variations from the equilibrium can be attributed to anharmonicities that can by construction not be captured by the classical FF. We emphasize that such deviations are associated with an energy of about 10 kJ/mol or higher, which corresponds to an equivalent temperature of 1200 K. In practice, MD simulations will be performed at much lower temperatures, and the deviations between FF₁ and the reference can be considered insignificant in this case.

3.1.2. Angle Bending. With the potential for the Py–T and Py–DPP bonds included in the FF, we now turn to the addition of the angle bending potentials. Figure 5 shows the

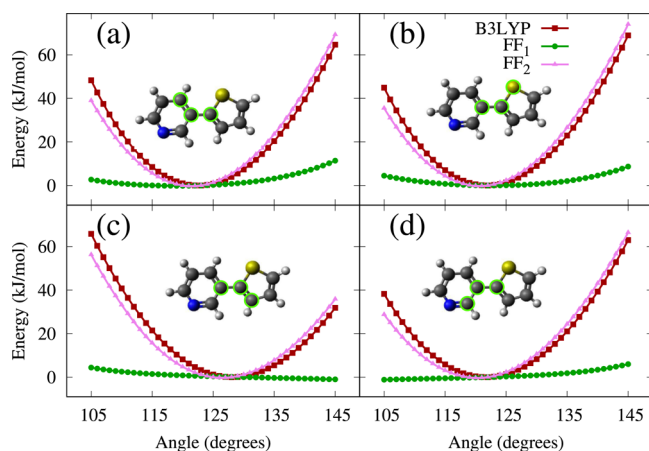


Figure 5. PES scans (in kJ/mol) for the angles (a) C1–C2–C4, (b) C2–C4–S, (c) C2–C4–C5, and (d) C3–C2–C4 in the Py–T structure, resulting from DFT/B3LYP (red squares), the FF₁ parameterization (green filled circles), and the updated FF₂ (pink filled triangles) FFs, respectively. The atoms defining the respective angles are also highlighted in the insets.

results of PES scans of the four angles in the Py–T structure based on the DFT/B3LYP reference and the FF₁ parameterization. The respective figure for the Py–DPP structure is shown as Figure S1 in the Supporting Information. However, the equilibrium angle and bending potential values are listed in Table 2. In contrast to the case of the bond potential, the

Table 2. Determined Harmonic Parameters for the Interfragment Angle Bending Potentials

	<i>i</i> – <i>j</i> – <i>k</i>	\tilde{k}_{ijk} (kJ/mol)	θ_{ijk}^0 (degree)
Py–T	C1–C2–C4	912.28	123
	C2–C4–S	807.07	122
	C2–C4–C5	802.55	128
	C3–C2–C4	896.77	122
Py–DPP	N1–C7–C8	2047.80	124
	C6–C7–C8	1860.80	127
	C7–C8–N2	1658.20	118
	C7–C8–C9	1623.20	120

harmonic force constants for the angle bending cannot be obtained from a simple fit of $\Delta V_{\text{angle}}(\theta_{ijk}) = V_{\text{angle}}^{\text{DFT}}(\theta_{ijk}) - V_{\text{angle}}^{\text{FF}_1}(\theta_{ijk})$ because the four angles are not independent of each other. Instead, we determine the eight unknown parameters (equilibrium angles θ_{ijk}^0 and force constants k_{ijk} for the four angles) simultaneously by minimizing the Frobenius norm of the matrix

$$F_{ijk,\alpha} = \Delta V_{\text{angle}}(\theta_{ijk,\alpha}) - \frac{1}{2}k_{ijk}(\theta_{ijk,\alpha} - \theta_{ijk}^0)^2 \quad (5)$$

where α indicates the angle values for which the PES has been scanned. Specifically, we used 41 points in the interval 105, 145°. In GROMOS-96, the angle potential is implemented in the form

$$V_{\text{angle}}(\theta_{ijk}) = \frac{1}{2}\tilde{k}_{ijk}(\cos(\theta_{ijk}) - \cos(\theta_{ijk}^0))^2 \quad (6)$$

where $\tilde{k}_{ijk} = k_{ijk}/\sin^2(\theta_{ijk}^0)$. The obtained parameters are given in Table 2. Adding these values and the corresponding equilibrium angles defines FF₂. The validation scan of the PES shown as pink triangles in Figure 5 shows good agreement

with the DFT/B3LYP reference. Similar to the bond potential, significant deviations are only observed that would occur at energies associated with extremely high equivalent temperatures and can therefore be considered insignificant for the intended applications in MD simulations of DPP2PymT.

3.1.3. Dihedral Angles. The final bonded potentials that remain to be determined are the periodic dihedrals formed by C1–C2–C4–S in Py–T and N1–C7–C8–N2 in Py–DPP. In Figure 6a, we show the PES scans for Py–T. The cis (trans)

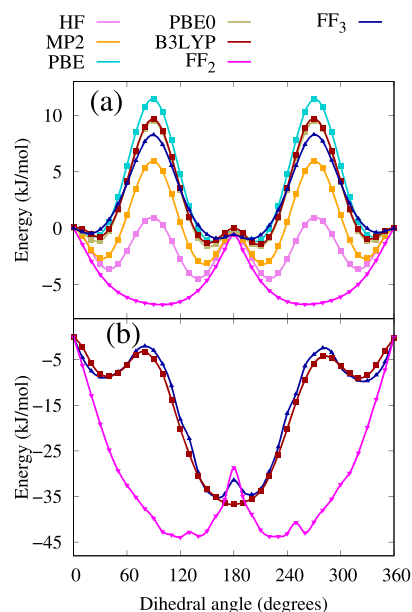


Figure 6. PES scan (in kJ/mol) for the (a) C1–C2–C4–S dihedral formed at the Py–T junction and (b) N1–C7–C8–N2 dihedral formed at the Py–DPP junction, resulting from DFT/B3LYP (red squares), the FF₃ parameterization (pink solid triangles), and the updated FF₃ (blue solid triangles) FFs, respectively. In (a), we also show PES scans from HF (magenta squares), MP2 (yellow squares), DFT/PBE, and DFT/PBE0. 0° is defined for the cis configuration with respect to the nitrogen of Py and sulfur of T, while 180° is the trans configuration. Similarly, cis is defined for the N1 of Py and N2 of DPP being on the same side and trans when they are opposite to each other.

orientation corresponds to 0° (180°), respectively. Without an explicit dihedral potential as in the FF₂ FF, an orthogonal arrangement of the Py and T fragments is preferred. In the DFT reference calculation, in contrast, a nearly planar conformation of Py–T is energetically most favorable, with the trans orientation slightly lower in energy by 0.67 kJ/mol. In both cases, there are two out-of-planarity conformations because of steric repulsion of the sulfur atom in thiophene and the hydrogen atom from the adjacent ring, separated by a barrier of 0.14 kJ/mol.⁴⁵ The energy barrier between cis and trans conformations, in contrast, is 10.5 kJ/mol.

To scrutinize the effect of the choice of the quantum mechanics (QM) method on the obtained PES in the parameterization procedure, we also performed additional PES scans with Hartree–Fock (HF), second-order Møller–Plesset perturbation theory (MP2), and DFT with the PBE and PBE0 functionals, as also shown in Figure 6a. We use this dihedral scan to illustrate the influence because the softer potentials are typically more sensitive to this choice.³⁰ All QM methods show a similar qualitative behavior regarding the

structure of the PES, as discussed above. Quantitatively, HF yields the lowest barrier between the cis and trans conformations (4.6 kJ/mol), which is about doubled when using MP2 (8.6 kJ/mol). The generalized-gradient PBE functional yields the highest barrier (12.1 kJ/mol) among the methods, nearly 3 times as large as in HF. Both hybrid functionals (PBE0 and B3LYP) are close to each other. Overall, the out-of-planarity conformations are separated by smaller barriers in all DFT methods compared to HF or MP2. As the cis–trans barrier is considered the most relevant for the torsional motion, we see that its B3LYP value is reasonably in good agreement with, for example, MP2, corroborating our choice of this functional for the parameterization of the FF. We also note that the DFT/B3LYP PES is converged with respect to the used basis set with def2-TZVP. As shown in Figure S2 of the Supporting Information, the PES calculated with def2-QZVP is practically indistinguishable.

For the Py–DPP dihedral, we observe minima at the FF₂ level (pink triangles in Figure 6b) in nonplanar trans orientations at 120 and 230°. The energy barrier is around 44 kJ/mol to the planar cis and 15 kJ/mol to the planar trans configuration. In the DFT/B3LYP reference, however, there is a clear absolute minimum at a 180° configuration and two local minima at 40 and 320°. For a transition from this twisted cis to the planar trans arrangement, a barrier of about 5 kJ/mol is found, while it is 32 kJ/mol for the inverse transition.

To obtain the classical potential associated with the dihedral rotation, the difference $\Delta V_{\text{dihedral}}(\phi_{ijkl}) = V_{\text{dihedral}}^{\text{DFT}}(\phi_{ijkl}) - V_{\text{dihedral}}^{\text{FF}_2}(\phi_{ijkl})$ is represented as

$$V_{\text{dihedral}}(\phi_{ijkl}) = k_{\phi}^{ijkl} [1 + (\cos(n\phi_{ijkl} - \delta_{ijkl}))] \quad (7)$$

where ϕ_{ijkl} is the value of the dihedral angle between the ijk and jkl planes, n is the multiplicity which arises because multiple points of minima can be obtained with a separation of a small energy barrier between 0 and 360°, and δ_{ijkl} is the phase shift. From the shape of both DFT/B3LYP reference curves (Py–T and Py–DPP), we see that they are symmetric about 180° and, hence, $n = 2$ and $\delta_{ijkl} = 180^\circ$. Adding the parameterized eq 7 as in Table 3 yields the updated FF FF₃.

Table 3. Determined Parameters for the Interfragment Periodic Dihedral Angle Potentials

	$i-j-k-l$	k_{ϕ}^{ijkl} (kJ/mol)	δ_{ijkl} (degree)
Py–T	C1–C2–C4–S	7.5	180
Py–DPP	N1–C7–C8–N2	18.50	180

A PES scan with this parameterization is shown as blue triangles in Figure 6. The overall shapes of the reference PES are reproduced, and FF₃ is a massive improvement over FF₂. Barrier heights, especially the one for the cis–trans transition in Py–T, are slightly underestimated, which is due to the limitations set by the functional form of eq 7.

3.1.4. Partial Charge Calculation. For the development of the interfragment bonded parameters, partial charges are assigned in Py–T and Py–DPP dimers as obtained with the CHELPG method³⁹ based on underlying DFT calculations. In general, the partial charges are determined based on the DFT-optimized geometries. In Figure S3 of the Supporting Information, we exemplarily illustrate the influence of different conformations of the Py–T dimer on the partial charge assignment. Charges determined on optimized geometries are compared to charges determined from all conformations in the

PES scan and a Boltzmann-weighted average at 300 K. While we note some variations in the charges, the Boltzmann-weighted average charges and the one from the optimized geometry are in good agreement. This corroborates the robustness of the partial charge determination in our FF. With all bonded parameters now at hand on the level of FF₃, we turn to refining the partial charges for the fully assembled molecule shown in Figure 1.

Once all the individual fragments are linked to form the DPP2PymT monomer, this step is necessary to account for changes in the charge distribution compared to one observed in the individual dimer structures. Special care needs to be taken regarding the terminating hydrogen atoms of the monomer residue: for a DPP2PymT that itself is located at the termini of the polymer, one hydrogen needs to be excluded from the CHELPG procedure, while any other residue does not contain hydrogen atoms at all at the inter-residue bond. To account for this, we perform three partial charge fits with the charge of either and both of the terminating hydrogen atoms constrained to 0. This will ensure charge neutrality of the polymer independent of the degree of polymerization. For simulations with addition of side chains, standard partial charge values as described in OPLS-AA were used.⁴⁶

Finally, with the definition of all bonded and nonbonded parameters for the DPP2PymT monomers at hand, the complete FF can be assembled for an arbitrary topology to perform MD simulations, as will be shown for the N_p -DPP2PymT polymer in solutions and as melts in the following sections.

3.2. N_p -DPP2PymT in Solution. We verify the quality of the FF using a series of polymer simulations, beginning in this section with a single-chain polymer simulation in vacuum, and then proceed to solvate the polymer chain in water and in chloroform to cross-check solvent effects as seen in experiments.

To begin with, a single polymer chain with the degree of polymerization $N_p = 50$ and 2-hexyldecyl side chains was simulated for each of the three polymer systems of $m = 1, 2, 3$. The simulation was started with the all-stretched chain conformation as shown in Figure 7, where the side chains are removed for visual clarity. This was put in a box of $105 \times 30 \times 30 \text{ nm}^3$ so that any artifacts in energy calculations arising from the polymer chain interacting with a mirror image of itself can be avoided. It was energy-minimized until the forces on

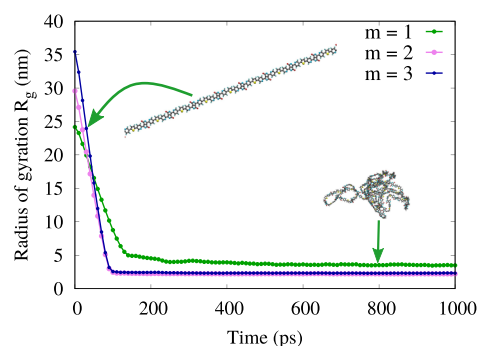


Figure 7. Radius of gyration (in nanometers) of 50-DPP2PymT in vacuum, starting from all-stretched chain conformations. Each chain collapses into a globule (see the inset in the bottom right) within the first 200 ps when simulated in the NVT ensemble at 300 K. Side chains have not been shown for visual clarity.

every atom were below 100 kJ/mol/nm. The integration time step used was 1 fs for 50-DPP2Py1T and 50-DPP2Py2T and 0.2 fs for 50-DPP2Py3T. Van der Waals interactions were cut off at 1.2 nm. Electrostatic interactions were evaluated using the particle-mesh Ewald⁴⁷ technique with a real space cutoff of 1.2 nm, a fourth-order interpolation, and a Fourier grid spacing of 0.16 nm. Upon simulating the structures in vacuum at 300 K in the *NVT* ensemble, using the velocity rescaling thermostat⁴⁸ with a time constant for the temperature coupling of 0.5 ps, the polymer chain collapsed within the first 200 ps into a globule, as shown in Figure 7. The systems are considered to be collapsed when the R_g value has stabilized.

The resulting collapsed polymer structure was then put into two different kinds of solvents to check for the solubility. Chloroform was used as the organic solvent (good) and water as the polar solvent (poor) for the simulations. We used the SPC/E water model⁴⁹ and the GROMOS FF for the chloroform solvent, respectively. The single polymer globule was solvated in 259,888 (59,495) molecules of water (chloroform) and equilibrated in a cubic box of $20 \times 20 \times 20$ nm³ with periodic boundary conditions. After energy minimization, simulations in the *NVT* ensemble were performed for 800 ps at room temperature (300 K). The solution was then simulated for 1 ns in the *NPT* ensemble maintaining the pressure at 1 atm using the Berendsen barostat⁵⁰ with a time constant for pressure coupling of 2 ps. These equilibration steps were followed by production runs for 5 ns in water and for up to 40 ns in chloroform. The calculations in water were stopped at 5 ns because there was no significant change in the values of R_g , as seen (green curve) in Figure 8. The calculations in chloroform yielded an increase in the values of R_g even after 30 ns for $m = 1, 3$. The resulting weight fractions (W_i) in the solution for different values of m are shown in Table 4.

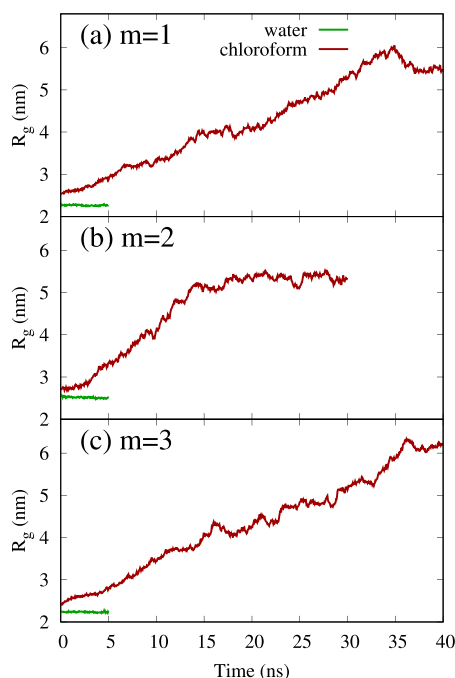


Figure 8. Radius of gyration of a single 50-DPP2PymT chain for $m = 1, 2, 3$ in water (green) and chloroform (red). Water is a poor solvent, and the polymer remains coiled, while in chloroform (a good solvent), swelling is clearly visible.

Table 4. Weight fraction (W_i) of the Polymer in Water and Chloroform Solution

	$m = 1$	$m = 2$	$m = 3$
W_i (water)	8.8×10^{-3}	9.6×10^{-3}	10.4×10^{-3}
W_i (chloroform)	5.8×10^{-3}	6.3×10^{-3}	6.9×10^{-3}

As is apparent from Figure 8, the simulations of the solvated polymer chains starting from the coiled conformations exhibit qualitatively contrasting behavior depending on the solvent: while the chain remains collapsed into the globule in water, it swells and eventually opens in chloroform. It has been well established that the intramolecular hydrogen bonding in the DPP compounds hinders its solubility in any kind of solvent. In order to have the DPP compounds solvated in water, their polarity needs to be enhanced by the addition of ionic functional groups⁵¹ or in some cases also by carboxylic acid functional groups.⁵² The absence of any such functional groups in the simulated polymers leads to the low solubility in water. In contrast, the addition of alkyl side chains, as has been implemented in the present simulations, enhances the solubility in organic solvents.¹⁴ This trend of solubility is well represented by the radius of gyration, R_g , in water and chloroform. We can see from Figure 8 that the values of R_g at $t = 0$ are different for the green curves and for the red curves. This is due to the fact that the polymer shows swelling characteristics in chloroform during *NVT* and *NPT* equilibration.

In order to analyze the solubility trend in more detail, we determine the solvent-accessible surface area (SASA) for the segment groups (DPP, thiophene, Py, and alkyl side chains) of the DPP2PymT polymer chains for $m = 1, 2, 3$, respectively. Figure 9 shows the SASA in water (left) and chloroform (right). We see that the surface areas for DPP, Py, and

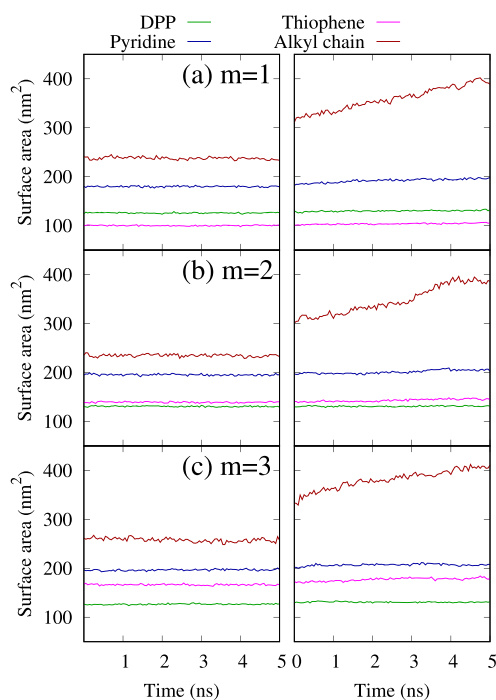


Figure 9. SASA (in nm²) for the individual segment types (DPP, thiophene, Py, and alkyl side chains) of single DPP2PymT polymer chains with $m = 1, 2, 3$ in water (left) and chloroform (right).

thiophenes, which form the backbone of the polymer chain, remain fairly constant for the duration of 5 ns in both water and chloroform. However, significant differences can be seen for the SASA of the alkyl chain. It remains constant in water, while it increases rapidly in chloroform. This is in line with the experimental findings, suggesting that the purpose of the side chains in DPP polymers is to aid in solubility in organic solvents, which results in the swelling of the polymer chain in chloroform.¹⁴

The above findings show that MD simulations of N_p -DPP2PymT in solutions yield qualitative results as expected from the literature, supporting the validity of the developed FF.

3.3. Melt Simulations. Conjugated polymers exhibit a significant change in structural characteristics at high temperatures.⁵³ As such structural changes often govern the performance of the polymer in optoelectronic devices,⁵⁴ we also carried out simulations of 50-DPP2PymT melts to study glass transition as well as the segmental mobility by analyzing torsional relaxations of the conjugated substituents.

3.3.1. Glass Transition. The initial configuration with the same degree of polymerization ($N_p = 50$) for polymer melt simulations has been created with 15 chains in their extended state. One single extended chain was aligned along the x -axis and duplicated 3 times along the y -axis and 5 times along the z -axis. The space between each chain was 5 nm. These chains were energy-minimized in a $105 \times 30 \times 30$ nm³ box until the forces on each atom converged to less than 100 kJ/mol/nm.

For similar DPP polymers without aromatic Py substituents, a melting temperature of about 550 K is known from the experiment.⁵⁵ We know as an empirical estimate that the glass-transition temperature (T_g) is approximately 2/3 of the melting temperature,⁵⁶ leading to an expected T_g of around 360 K. We therefore assume that a temperature of 600 K is sufficiently high to simulate the 50-DPP2PymT melts initially above T_g . In particular, the melts are first simulated for 2 ns in the NVT ensemble at 600 K using the velocity rescaling⁴⁸ thermostat with a time constant of 0.5 ps. The resulting structure from the NVT run was simulated at 1 atm in the NPT ensemble. The pressure was maintained using the Berendsen barostat⁵⁰ with a constant for pressure coupling of 2.0 ps until we observed a stable density. These equilibrated systems were then cooled from 600 to 100 K at a cooling velocity of 10 K/ns to determine the glass-transition temperatures. This cooling rate is orders of magnitude higher than the experimental one, which is computationally infeasible to reach within a reasonable amount of time. In general, higher cooling rates lead to higher T_g ^{57,58} so that our results are expected to overestimate the experimental glass transition slightly.

Figure 10 shows the cooling curves for the three polymers. The melt densities at 600 K increase significantly with the number of thiophene units, amounting to 923, 973, and 1005 kg/m³ for $m = 1, 2, 3$, respectively. Glass-transition temperatures are extracted as the intersection of linear temperature dependence of the density fitted in the regions clearly below (from 100 to 200 K) and above (from 500 to 600 K) T_g . It is clear from Figure 10 that the transition is not very definite and occurs gradually, and the glass-transition temperatures are obtained as (357 ± 30) K for $m = 1$, (346 ± 30) K for $m = 2$, and (366 ± 20) K for $m = 3$.

3.3.2. Segmental Mobility. With the details about the glass transition at hand, we study the conformational mobility and isomerization rates of the substituents in the polymer backbone at various temperatures, both above and below T_g .

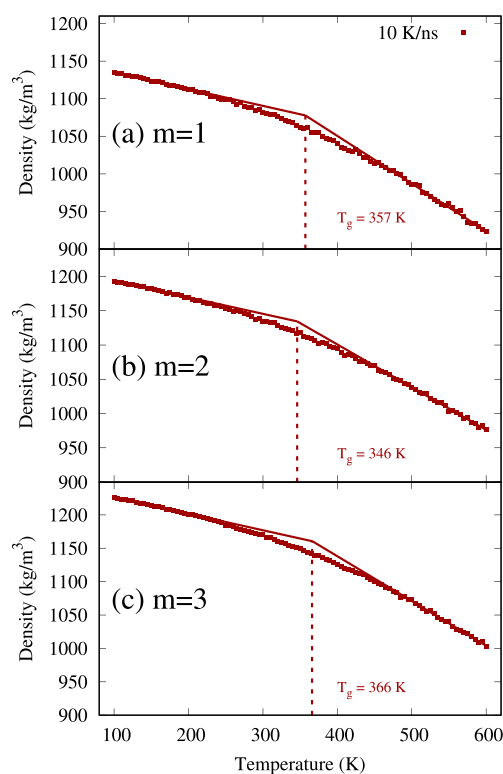


Figure 10. Temperature dependence of the density of the 50-DPP2PymT melt ($m = 1, 2, 3$) for a cooling rate of 10 K/ns. Linear fits to the data at low (from 100 to 200 K) and high (from 500 to 600 K) temperatures are used to obtain glass-transition temperatures of (357 ± 30) K for $m = 1$, (346 ± 30) K for $m = 2$, and (366 ± 20) K for $m = 3$.

To this end, we determine the torsional autocorrelation function (TACF) and analyze its characteristic time decay. We used snapshots from the 10 K/ns cooling simulation for the starting structures. The structures were taken between 600 and 250 K at an interval of 50 K. Energy minimization and NVT and NPT equilibration for 200 ps were carried out on the starting structures at each temperature. This was followed by a production run for 1 ns in the NPT ensemble. We study the segmental relaxation using a normalized autocorrelation function.

$$R_{\phi}(t) = \frac{\langle \cos \phi_i(t) \cos \phi_i(0) \rangle - \langle \cos \phi_i(0) \rangle^2}{\langle \cos \phi_i(0) \cos \phi_i(0) \rangle - \langle \cos \phi_i(0) \rangle^2} \quad (8)$$

where $\cos \phi_i(t)$ and $\cos \phi_i(0)$ are the torsional angles at time t and at start of the simulation, respectively.

The autocorrelation for Py–thiophene (Py–T1) and thiophene–thiophene (T1–T2 and T2–T3) dihedrals at 300 and 500 K are shown in Figure 11 for $m = 1, 2, 3$. At 300 K, the TACFs for all dihedrals relax only a little, remaining at values above 0.9 at large times, indicating very little change in the relative arrangement of the involved conjugated segments during 1 ns. The observation that the T–T dihedrals show slightly more relaxation than Py–T can be attributed to the minimally softer potential and a barrier-free minimum in the former case.³⁰ In contrast, at 500 K, the differences between Py–T1 and T1–T2 are not very prominent. Both show, after an initial fast decay, a second much slower component, which is not discernible below the glass-transition temperature.

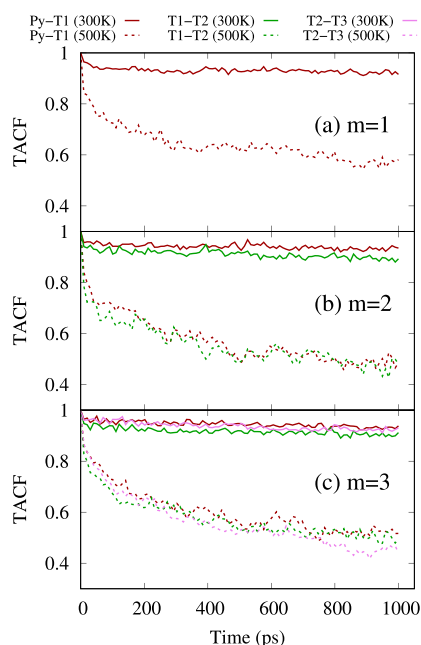


Figure 11. TACF plots between Py–T1 (red), T1–T2 (green), and T2–T3 (violet) rings for the DPP2PymT polymer. The solid lines depict the values at 300 K, while the dashed lines represent values at 500 K. The TACF values are the average of all the 750 dihedrals of one kind formed with 15 polymer chains of 50-DPP2PymT.

The TACFs clearly point to two characteristic relaxation processes: a rapid one with a small relaxation time τ_r , corresponding to the torsional vibrations around the minima of the dihedral potential, and a slow one with a large τ_s , corresponding to cis–trans transitions with energy barriers as discussed in Section 3.1.3. Hence, we determine both relaxation times and the activation energy for torsional relaxations by fitting a sum of two exponentials to the TACFs. The τ_r increases with temperature and typically ranges between 5 and 20 ps below and between 30 and 100 ps above the glass-transition temperature for both the Py–T (Py–thiophene) dihedral and T–T (thiophene–thiophene) dihedrals.

For the slow relaxation process, τ_s ranges between 10^3 and 10^4 ps at higher temperatures, while it is well above 10^5 ps for the lower end of the temperature scale. In Figure 12, we see that at low temperatures, the logarithm of τ_s is inversely

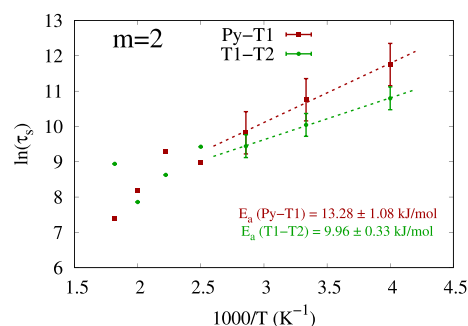


Figure 12. Logarithm of the relaxation times vs inverse of temperature for DPP2Py2T. Linear fitting has been done at temperatures above the glass transition to extract the activation energy for segmental relaxations. The activation energies are shown on the bottom right for Py–T1 and T1–T2 segmental relaxations.

proportional to the temperature, as expected by the Arrhenius equation $\tau = \tau_0 \exp(E_a/RT)$, which holds for polymers below their glass-transition temperature. From linear fits in this temperature range, we obtain activation energies for the segmental relaxation of (13.3 ± 1.1) kJ/mol for the Py–T1 dihedral and (9.7 ± 0.3) kJ/mol for the T1–T2 dihedral.

These values are qualitatively in correspondence to the dihedral barriers we obtain from FF parameterization and indicate that the torsional motion is the driving mechanism for polymer relaxation and segmental mobility.

4. SUMMARY

In this paper, we develop an all-atom FF for DPP2PymT for $m = 1, 2, 3$ by linking the individual fragments that form the building blocks for the polymer. We determine bonded parameters using DFT methods and electrostatic parameters using the CHELPG scheme. This developed FF is validated using a series of solution and melt simulations. Qualitative conclusions drawn from the solution simulations were in line with the well-established fact that chloroform acts as a good solvent for DPP polymers with alkyl side chains, while water shows poor solvent characteristics. The polymer melt provided reasonable values for the glass-transition temperature ranging between 340 and 370 K. As a final check, we also looked at the autocorrelation function for torsional decay which corroborated well with our FF parameters and softer dihedrals relaxed with lower relaxation times.

■ ASSOCIATED CONTENT

Supporting Information

The Supporting Information is available free of charge at <https://pubs.acs.org/doi/10.1021/acs.jpcc.0c06787>.

PES scans of Py–DPP angles, PES scans of the Py–T dihedral for different basis sets, comparison of partial charges for the Py–T dimer from different methods, DPP2PymT chains in water and chloroform, and instructions to access the fully assembled FF files for 50-DPP2PymT in the GROMACS format (PDF)

■ AUTHOR INFORMATION

Corresponding Author

Björn Baumeier – Department of Mathematics and Computer Science and Institute for Complex Molecular Systems, Eindhoven University of Technology, 5600 MB Eindhoven, The Netherlands; orcid.org/0000-0002-6077-0467; Email: b.baumeier@tue.nl

Authors

Vivek Sundaram – Department of Mathematics and Computer Science, Department of Applied Physics, and Institute for Complex Molecular Systems, Eindhoven University of Technology, 5600 MB Eindhoven, The Netherlands

Alexey V. Lyulin – Department of Applied Physics, Eindhoven University of Technology, 5600 MB Eindhoven, The Netherlands; orcid.org/0000-0002-7533-3366

Complete contact information is available at:

<https://pubs.acs.org/doi/10.1021/acs.jpcc.0c06787>

Notes

The authors declare no competing financial interest.

ACKNOWLEDGMENTS

Funding for this work was provided by the Netherlands Organisation for Scientific Research (NWO) and the Netherlands eScience Center through project number 027.017.G15, within the Joint CSER and eScience program for Energy Research (JCER 2017). B.B. also acknowledges support by the Innovational Research Incentives Scheme Vidi of the NWO with project number 723.016.002.

REFERENCES

- (1) Shockley, W.; Queisser, H. J.; Ell, R. Detailed Balance Limit of Efficiency of pn Junction Solar Cells. *J. Appl. Phys.* **1961**, *32*, 510.
- (2) Rühle, S. Tabulated values of the Shockley-Queisser limit for single junction solar cells. *Sol. Energy* **2016**, *130*, 139–147.
- (3) Andreani, L. C.; Bozzola, A.; Kowalczewski, P.; Liscidini, M.; Redorici, L. Silicon solar cells: toward the efficiency limits. *Adv. Phys.: X* **2019**, *4*, 1548305.
- (4) Li, W.; Hendriks, K. H.; Wienk, M. M.; Janssen, R. A. J. Diketopyrrolopyrrole Polymers for Organic Solar Cells. *Acc. Chem. Res.* **2016**, *49*, 78–85.
- (5) Zhao, J.; Wang, A.; Green, M. A.; Ferrazza, F. 19.8% efficient "honeycomb" textured multicrystalline and 24.4% monocrystalline silicon solar cells. *Appl. Phys. Lett.* **1998**, *73*, 1991–1993.
- (6) Shah, A.; Torres, P.; Tschamer, R.; Wyrsh, N.; Keppner, H. Photovoltaic technology: The case for thin-film solar cells. *Science* **1999**, *285*, 692–698.
- (7) Sai, H.; Matsui, T.; Matsubara, K. Stabilized 14.0%-efficient triple-junction thin-film silicon solar cell. *Appl. Phys. Lett.* **2016**, *109*, 183506.
- (8) Qarony, W.; Hossain, M. I.; Hossain, M. K.; Uddin, M. J.; Haque, A.; Saad, A. R.; Tsang, Y. H. Efficient amorphous silicon solar cells: characterization, optimization, and optical loss analysis. *Results Phys.* **2017**, *7*, 4287–4293.
- (9) Duan, C.; Huang, F.; Cao, Y. Recent development of push-pull conjugated polymers for bulk-heterojunction photovoltaics: Rational design and fine tailoring of molecular structures. *J. Mater. Chem.* **2012**, *22*, 10416–10434.
- (10) Thompson, B. C.; Fréchet, J. M. J. Polymer-fullerene composite solar cells. *Angew. Chem. Int. Ed.* **2008**, *47*, 58–77.
- (11) Liang, Y.; Feng, D.; Wu, Y.; Tsai, S.-T.; Li, G.; Ray, C.; Yu, L. Highly efficient solar cell polymers developed via fine-tuning of structural and electronic properties. *J. Am. Chem. Soc.* **2009**, *131*, 7792–7799.
- (12) Su, M.-S.; Kuo, C.-Y.; Yuan, M.-C.; Jeng, U.-S.; Su, C.-J.; Wei, K.-H. Improving device efficiency of polymer/fullerene bulk heterojunction solar cells through enhanced crystallinity and reduced grain boundaries induced by solvent additives. *Adv. Mater.* **2011**, *23*, 3315–3319.
- (13) Wienk, M. M.; Turbiez, M.; Gilot, J.; Janssen, R. A. J. Narrow-bandgap diketopyrrolo-pyrrole polymer solar cells: The effect of processing on the performance. *Adv. Mater.* **2008**, *20*, 2556–2560.
- (14) Chandran, D.; Lee, K.-S. Diketopyrrolopyrrole: A Versatile Building Block for Organic Photovoltaic Materials. *Macromol. Res.* **2013**, *21*, 272–283.
- (15) Chapin, D. M.; Fuller, C. S.; Pearson, G. L. A new silicon p-n junction photocell for converting solar radiation into electrical power. *J. Appl. Phys.* **1954**, *25*, 676–677.
- (16) Choi, H.; Ko, S.-J.; Kim, T.; Morin, P.-O.; Walker, B.; Lee, B. H.; Leclerc, M.; Kim, J. Y.; Heeger, A. J. Small-bandgap polymer solar cells with unprecedented short-circuit current density and high fill factor. *Adv. Mater.* **2015**, *27*, 3318–3324.
- (17) Ashraf, R. S.; Meager, I.; Nikolka, M.; Kirkus, M.; Planells, M.; Schroeder, B. C.; Holliday, S.; Hurhangee, M.; Nielsen, C. B.; Sirringhaus, H.; et al. Chalcogenophene comonomer comparison in small band gap diketopyrrolopyrrole-based conjugated polymers for high-performing field-effect transistors and organic solar cells. *J. Am. Chem. Soc.* **2015**, *137*, 1314–1321.
- (18) Hendriks, K. H.; Heintges, G. H. L.; Gevaerts, V. S.; Wienk, M. M.; Janssen, R. A. J. High-molecular-weight regular alternating diketopyrrolopyrrole-based terpolymers for efficient organic solar cells. *Angew. Chem. Int. Ed.* **2013**, *52*, 8341–8344.
- (19) Heinrichová, P.; Pospíšil, J.; Štriteský, S.; Vala, M.; Weiter, M.; Toman, P.; Rais, D.; Pflieger, J.; Vondráček, M.; Šimek, D.; et al. Diketopyrrolopyrrole-Based Organic Solar Cells Functionality: The Role of Orbital Energy and Crystallinity. *J. Phys. Chem. C* **2019**, *123*, 11447–11463.
- (20) Wehner, J.; Baumeier, B. Multiscale simulations of singlet and triplet exciton dynamics in energetically disordered molecular systems based on many-body Green's functions theory Multiscale simulations of singlet and triplet exciton dynamics in energetically disordered molecular systems. *New J. Phys.* **2020**, *22*, 033033.
- (21) Wehner, J.; Brombacher, L.; Brown, J.; Jungmans, C.; Çaylak, O.; Khalak, Y.; Madhikar, P.; Tirimbò, G.; Baumeier, B. Electronic Excitations in Complex Molecular Environments: Many-Body Green's Functions Theory in VOTCA-XTP. *J. Chem. Theory Comput.* **2018**, *14*, 6253–6268.
- (22) Li, J.; D'Avino, G.; Duchemin, I.; Beljonne, D.; Blase, X. Combining the Many-Body GW Formalism with Classical Polarizable Models: Insights on the Electronic Structure of Molecular Solids. *J. Phys. Chem. Lett.* **2016**, *7*, 2814–2820.
- (23) de Vries, X.; Friederich, P.; Wenzel, W.; Coehoorn, R.; Bobbert, P. A. Full quantum treatment of charge dynamics in amorphous molecular semiconductors. *Phys. Rev. B: Condens. Matter Mater. Phys.* **2018**, *97*, 075203.
- (24) Rühle, V.; Lukyanov, A.; May, F.; Schrader, M.; Vehoff, T.; Kirkpatrick, J.; Baumeier, B.; Andrienko, D. Microscopic simulations of charge transport in disordered organic semiconductors. *J. Chem. Theory Comput.* **2011**, *7*, 3335–3345.
- (25) Tirimbò, G.; Sundaram, V.; Çaylak, O.; Scharpach, W.; Sijen, J.; Jungmans, C.; Brown, J.; Ruiz, F. Z.; Renaud, N.; Wehner, J.; et al. Excited-state electronic structure of molecules using many-body Green's functions: Quasiparticles and electron-hole excitations with VOTCA-XTP. *J. Chem. Phys.* **2020**, *152*, 114103.
- (26) Guerrero, A.; Garcia-Belmonte, G. Recent advances to understand morphology stability of organic photovoltaics. *Nano-Micro Lett.* **2017**, *9*, 10.
- (27) Savikhin, V.; Babics, M.; Neophytou, M.; Liu, S.; Oosterhout, S. D.; Yan, H.; Gu, X.; Beaujuge, P. M.; Toney, M. F. Impact of Polymer Side Chain Modification on OPV Morphology and Performance. *Chem. Mater.* **2018**, *30*, 7872–7884.
- (28) Grozema, F. C.; Van Duijnen, P. T.; Berlin, Y. A.; Ratner, M. A.; Siebbeles, L. D. A. Intramolecular charge transport along isolated chains of conjugated polymers: Effect of torsional disorder and polymerization defects. *J. Phys. Chem. B* **2002**, *106*, 7791–7795.
- (29) Hendriks, K. H.; Wijkema, A. S. G.; Van Franeker, J. J.; Wienk, M. M.; Janssen, R. A. J. Dichotomous Role of Exciting the Donor or the Acceptor on Charge Generation in Organic Solar Cells. *J. Am. Chem. Soc.* **2016**, *138*, 10026–10031.
- (30) Wildman, J.; Repiščák, P.; Paterson, M. J.; Galbraith, I. General Force-Field Parametrization Scheme for Molecular Dynamics Simulations of Conjugated Materials in Solution. *J. Chem. Theory Comput.* **2016**, *12*, 3813–3824.
- (31) Zoete, V.; Cuendet, M. A.; Grosdidier, A.; Michielin, O. SwissParam: A fast force field generation tool for small organic molecules. *J. Comput. Chem.* **2011**, *32*, 2359–2368.
- (32) Vanommeslaeghe, K.; Raman, E. P.; MacKerell, A. D. Automation of the CHARMM General Force Field (CGenFF) II: Assignment of Bonded Parameters and Partial Atomic Charges. *J. Chem. Inf. Model.* **2012**, *52*, 3155–3168.
- (33) Ramos Sasselli, I.; Ulijn, R. V.; Tuttle, T. CHARMM force field parameterization protocol for self-assembling peptide amphiphiles: The Fmoc moiety. *Phys. Chem. Chem. Phys.* **2016**, *18*, 4659–4667.
- (34) Dodda, L. S.; Cabeza de Vaca, I.; Tirado-Rives, J.; Jorgensen, W. L. LigParGen web server: An automatic OPLS-AA parameter generator for organic ligands. *Nucleic Acids Res.* **2017**, *45*, W331–W336.

- (35) Schmid, N.; Eichenberger, A. P.; Choutko, A.; Riniker, S.; Winger, M.; Mark, A. E.; Van Gunsteren, W. F. Definition and testing of the GROMOS force-field versions 54A7 and 54B7. *Eur. Biophys. J.* **2011**, *40*, 843–856.
- (36) Malde, A. K.; Zuo, L.; Breeze, M.; Stroet, M.; Poger, D.; Nair, P. C.; Oostenbrink, C.; Mark, A. E. An Automated Force Field Topology Builder (ATB) and Repository: Version 1.0. *J. Chem. Theory Comput.* **2011**, *7*, 4026–4037.
- (37) Singh, U. C.; Kollman, P. A. An approach to computing electrostatic charges for molecules. *J. Comput. Chem.* **1984**, *5*, 129–145.
- (38) Scott, W. R. P.; Hünenberger, P. H.; Tironi, I. G.; Mark, A. E.; Billeter, S. R.; Fennen, J.; Torda, A. E.; Huber, T.; Krüger, P.; Van Gunsteren, W. F. The GROMOS biomolecular simulation program package. *J. Phys. Chem. A* **1999**, *103*, 3596–3607.
- (39) Breneman, C. M.; Wiberg, K. B. Determining atom-centered monopoles from molecular electrostatic potentials. The need for high sampling density in formamide conformational analysis. *J. Comput. Chem.* **1990**, *11*, 361–373.
- (40) Neese, F. The ORCA program system. *Wiley Interdiscip. Rev.: Comput. Mol. Sci.* **2012**, *2*, 73–78.
- (41) Yanai, T.; Tew, D. P.; Handy, N. C. A new hybrid exchange-correlation functional using the Coulomb-attenuating method (CAM-B3LYP). *Chem. Phys. Lett.* **2004**, *393*, 51–57.
- (42) Weigend, F.; Häser, M.; Patzelt, H.; Ahlrichs, R. RI-MP2: Optimized auxiliary basis sets and demonstration of efficiency. *Chem. Phys. Lett.* **1998**, *294*, 143–152.
- (43) Bekker, H.; Berendsen, H.; Dijkstara, E.; Achterop, S.; Vondrumen, R.; Vanderspoel, D.; Sijbers, A.; Keegstra, H.; Renardus, M. *GROMACS—A Parallel Computer for Molecular-Dynamics Simulations*; World Scientific Publishing: Singapore, 1993; pp 252–256.
- (44) Abraham, M. J.; Murtola, T.; Schulz, R.; Páll, S.; Smith, J. C.; Hess, B.; Lindahl, E. Gromacs: High performance molecular simulations through multi-level parallelism from laptops to supercomputers. *SoftwareX* **2015**, *1–2*, 19–25.
- (45) Zade, S. S.; Bendikov, M. Twisting of conjugated oligomers and polymers: Case study of oligo- And polythiophene. *Chem.—Eur. J.* **2007**, *13*, 3688–3700.
- (46) Jorgensen, W. L.; Tirado-Rives, J. The OPLS Potential Functions for Proteins. Energy Minimizations for Crystals of Cyclic Peptides and Crambin. *J. Am. Chem. Soc.* **1988**, *110*, 1657–1666.
- (47) Darden, T.; York, D.; Pedersen, L. Particle mesh Ewald: An $N \log(N)$ method for Ewald sums in large systems. *J. Chem. Phys.* **1993**, *98*, 10089–10092.
- (48) Bussi, G.; Donadio, D.; Parrinello, M. Canonical sampling through velocity rescaling. *J. Chem. Phys.* **2007**, *126*, 014101.
- (49) Berendsen, H. J. C.; Grigera, J. R.; Straatsma, T. P. The Missing Term in Effective Pair Potentials. *J. Phys. Chem.* **1987**, *91*, 6269–6271.
- (50) Berendsen, H. J. C.; Postma, J. P. M.; Van Gunsteren, W. F.; Dinola, A.; Haak, J. R. Molecular dynamics with coupling to an external bath. *J. Chem. Phys.* **1984**, *81*, 3684–3690.
- (51) Grzybowski, M.; Glodkowska-Mrowka, E.; Clermont, G.; Blanchard-Desce, M.; Gryko, D. T. Synthesis and optical properties of water-soluble diketopyrrolopyrroles. *Chem. Heterocycl. Compd.* **2017**, *53*, 72–77.
- (52) Tang, S.; Ghazvini Zadeh, E. H.; Kim, B.; Toomey, N. T.; Bondar, M. V.; Belfield, K. D. Protein-induced fluorescence enhancement of two-photon excitable water-soluble diketopyrrolopyrroles. *Org. Biomol. Chem.* **2017**, *15*, 6511–6519.
- (53) Xie, R.; Lee, Y.; Aplan, M. P.; Caggiano, N. J.; Müller, C.; Colby, R. H.; Gomez, E. D. Glass Transition Temperature of Conjugated Polymers by Oscillatory Shear Rheometry. *Macromolecules* **2017**, *50*, 5146–5154.
- (54) Leman, D.; Kelly, M. A.; Ness, S.; Engmann, S.; Herzing, A.; Snyder, C.; Ro, H. W.; Kline, R. J.; DeLongchamp, D. M.; Richter, L. J. In situ characterization of polymer-fullerene bilayer stability. *Macromolecules* **2015**, *48*, 383–392.
- (55) Luo, S.; Wang, T.; Ocheje, M. U.; Zhang, S.; Xu, J.; Qian, Z.; Gu, X.; Xue, G.; Rondeau-Gagné, S.; Jiang, J.; et al. Multiamorphous Phases in Diketopyrrolopyrrole-Based Conjugated Polymers: From Bulk to Ultrathin Films. *Macromolecules* **2020**, *53*, 4480–4489.
- (56) Sakka, S.; Mackenzie, J. D. Relation between apparent glass transition temperature and liquids temperature for inorganic glasses. *J. Non-Cryst. Solids* **1971**, *6*, 145–162.
- (57) Lyulin, A. V.; Balabaev, N. K.; Michels, M. A. J. Molecular-weight and cooling-rate dependence of simulated Tg for amorphous polystyrene. *Macromol* **2003**, *36*, 8574–8575.
- (58) Barrat, J.-L.; Baschnagel, J.; Lyulin, A. Molecular dynamics simulations of glassy polymers. *Soft Matter* **2010**, *6*, 3430–3446.